J Adv Ceram

Research Article

Isotropic hexagonal boron nitride ceramics with high thermal conductivity and strength

Meng Hu[1], Wenyuan Zhang[1], Jixiang Zhang[1], Mengdong Ma[2,✉], Penghui Li[2], Shuai Chen[2], Yingju Wu[3,✉], Yan Zhong[1], Julong He[2], Ralf Riedel[4], Jianning Ding[1]

Cite this article: Hu M, Zhang W, Zhang J, et al. *J Adv Ceram* 2026, **15**(4): 9221275. https://doi.org/10.26599/JAC.2026.9221275

ABSTRACT: The conventional fabrication of bulk van der Waals materials, such as hexagonal boron nitride (hBN), faces significant challenges in sintering powder into structurally isotropic bulk forms. hBN has attracted considerable attention for applications under extreme conditions because of its excellent thermal stability, oxidation resistance, and electrical insulation. However, its strongly anisotropic layered structure typically results in poor mechanical performance and limited isotropy in bulk forms. In this study, we report the fabrication of isotropic hBN ceramics through the controlled transformation of cubic BN (cBN) powders under spark plasma sintering conditions. The coexistence of randomly oriented hBN sheets and residual turbostratic BN (tBN) phases produces an isotropic microstructure that yields balanced mechanical and thermal properties. The ceramics exhibit a compressive strength of ~130 MPa and a thermal conductivity of ~77 W·m^{-1}·K^{-1}, nearly independent of the measurement direction. This thermally driven cBN → hBN transformation provides a new strategy for tailoring the microstructure and overcoming the intrinsic anisotropy of layered ceramics, paving the way for advanced insulating components in harsh environments.

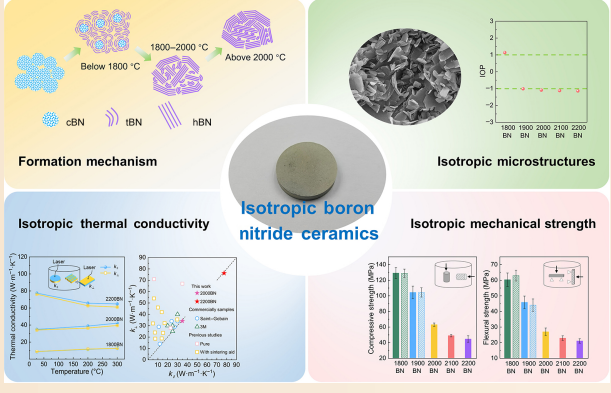

KEYWORDS: hexagonal boron nitride (hBN) ceramics; structurally isotropic; phase transformation; thermal conductivity; mechanical properties

1 Introduction

Hexagonal boron nitride (hBN) is a competitive candidate for efficient and safe heat spreaders in next-generation miniaturized electronic circuits, particularly for high-end electronic devices [1–3]. However, a major challenge lies in achieving isotropic thermal conductivity in hBN bulks. As an atomically layered two-dimensional material, the atoms within its layers are bonded by strong covalent bonds, while the atomic layers are connected by weak van der Waals interactions. Such bonding anisotropy directly leads to marked differences in the thermal conductivity and mechanical properties of the hBN single crystal between its in-plane and interlayer directions [4,5]. Moreover, polycrystalline hBN bulk ceramics fabricated via powder sintering also typically exhibit significant anisotropy in both their microstructure and physical properties. The anisotropic crystal structure of hBN results in an extremely low interlayer atomic diffusion coefficient. During high-temperature sintering, it is difficult for atoms to effectively migrate and eliminate pores, resulting in low-density ceramic bulks with inferior properties that fail to meet application requirements. Therefore, dense hBN ceramics with desirable properties are typically produced via pressure-assisted sintering processes. In such processes, the intrinsic anisotropic nature of hBN drives its *c*-axis to preferentially align along the direction of the sintering pressure, thereby forming a highly textured microstructure and anisotropic physical properties [6–8]. Therefore, developing isotropic hBN ceramics that combine high density with outstanding isotropic performance has always been a key research focus in the field.

To mitigate the anisotropy in hBN ceramics, various strategies have been explored, including reducing the grain size of the precursor, optimizing the sintering temperature and pressure parameters, and incorporating a secondary phase. For example, Niu *et al.* [9] fabricated a series of hBN/magnesium aluminum

[1] School of Mechanical Engineering, Jiangsu University, Zhenjiang 212013, China. [2] Center for High Pressure Science, State Key Laboratory of Metastable Materials Science and Technology, Yanshan University, Qinhuangdao 066004, China. [3] Mechano-X Institute, Applied Mechanics Laboratory, Department of Engineering Mechanics, Tsinghua University, Beijing 100084, China. [4] Institute of Materials Science, Technical University of Darmstadt, Darmstadt 64287, Germany.

✉ Corresponding authors. E-mail: M. Ma, mamengdong@ysu.edu.cn; Y. Wu, yingjuwu@mail.tsinghua.edu.cn

Received: November 15, 2025; Revised: February 15, 2026; Accepted: March 2, 2026

silicate (MAS) composites by sintering hBN particles with different sizes. Their experimental analysis revealed that as the precursor particle size decreases from 11 to 0.5 μm, the index of orientation preference (IOP, a critical quantitative indicator of texture degree) drops from −5413.6 to −16.7. Duan *et al.* [10] synthesized hBN ceramics by using ball-milled hBN powders with a grain size of 200–300 nm and reducing the holding times during hot-press sintering. This approach suppressed grain growth, yielding a weakly textured microstructure with an IOP of approximately −15. Zhang *et al.* [11] obtained hBN composite ceramics with an IOP reduced to −5.21 by incorporating glass phases as both sintering aids and reinforcing phases. However, it is worth noting that these hBN ceramics and composite ceramics with reduced texture degree still exhibit significant anisotropy in mechanical and thermal properties. Specifically, the thermal conductivity and flexural strength measured along directions perpendicular and parallel to the sintering pressure differ by more than a factor of two [9,11]. Thus, achieving structurally isotropic hBN bulk ceramics with isotropic thermal and mechanical properties remains a significant challenge in hBN development.

Boron nitride (BN) exhibits a wide variety of structural polymorphs (Fig. S1 in the Electronic Supplementary Material (ESM)), including hBN, cubic boron nitride (cBN), turbostratic boron nitride (tBN, disordered layer stacking), onion-like boron nitride (oBN), wurtzite boron nitride (wBN), and rhombohedral boron nitride (rBN). The interconversion of BN polymorphs, driven by thermodynamic and kinetic factors, has become a powerful strategy for fabricating high-performance BN bulk ceramics with exceptional properties. For example, tBN was fabricated into dense BN bulk ceramics exhibiting higher bending strength, Young's modulus, and hardness than conventionally consolidated hBN [12]. oBN was compressed under high pressures up to 15 GPa to yield nanotwinned cBN with ultrahigh hardness rivalling that of synthetic diamond [13]. Under spark plasma sintering (SPS), oBN was transformed into a kind of BN ceramic with twisted-layered structures, exhibiting a room-temperature compressive strain of up to 14% and a permanent plastic deformation of 8% [14]. Due to the complex growth kinetics [15], the sintering behavior of cBN is highly dependent on grain size and processing parameters. For cBN with grain sizes of 1–2 μm, partial transformation into hBN occurred at 90 MPa and 1500 °C, with complete conversion achieved at 1700 °C [16]. Following the complete transformation, the sintered hBN exhibited a Young's modulus of 10.47 GPa, approximately three times that of hBN powder sintered under identical conditions. In contrast, cBN with grain sizes of 200–400 nm underwent a complete phase transformation at 80 MPa and 1400 °C with the formation of oBN [17]. This transformation reduced the structural anisotropy of the sintered hBN bulks and further enhanced the Young's modulus to 29.44 GPa. The diversity in phase transformation pathways and resulting products offers potential for synthesizing high-performance BN ceramics derived from cBN.

In this study, we synthesized bulk hBN ceramics with an isotropic microstructure and physical properties by controlled thermal conversion of cBN under high-temperature conditions. We systematically investigate the microstructural evolution, phase composition, and mechanical and thermal properties. The results reveal that partial retention of tBN together with randomly stacked hBN sheets yields isotropic behavior in both mechanical strength and thermal conductivity, providing new insights into the design of high-performance BN ceramics.

2 Experimental

2.1 Material and synthesis

cBN powder (Apinno, China, average grain size of 50 nm) was employed as the raw material. The synthesis procedure is schematically illustrated in Fig. S2 in the ESM. Prior to sintering, the powder was treated with 5 wt% hydrochloric acid for 10 h to remove impurities such as boron oxide (B_2O_3), thereby avoiding their adverse effects on sintering. The acid-washed powder was then rinsed with deionized water until neutral, followed by vacuum drying at 80 °C to remove residual moisture. The dried cBN was ground into fine powders for sintering on an SPS system (FHP-828, Suzhou Haatn, China). SPS is a rapid powder consolidation process that uses electric current to densify ceramic or metal powders. Compared with conventional pressure sintering methods, SPS enables faster densification at lower temperatures, thereby preserving fine microstructures and controlling phase transformations. The sintering pressure was set at 15 MPa, as this low pressure facilitates industrial-scale production and enables the fabrication of larger products. Meanwhile, lower pressure is also beneficial for reducing the anisotropy of sintered blocks. The samples were consolidated at temperatures of 1500, 1600, 1700, 1800, 1900, 2000, 2100, and 2200 °C, with a heating rate of 100 °C·min^{-1}. The entire sintering process was carried out in an argon atmosphere, with a 10-min holding time at the target temperature before pressure release. Subsequently, the samples were cooled to room temperature within the chamber before being removed. The recovered samples were ground and polished for further microstructural and performance characterization. The samples were designated as 1500BN, 1600BN, 1700BN, 1800BN, 1900BN, 2000BN, 2100BN, and 2200BN based on their sintering temperature. For comparison, hBN ceramic (labeled hBN-2200) was prepared by SPS of hBN powder (150 nm, Sigma Aldrich) under the same conditions (15 MPa and 2200 °C). In addition, a sample labeled HP-1900 was obtained by hot-pressing cBN at 1900 °C and 15 MPa with a holding time of 10 min using an FVPHP-R-10 furnace (Fuji Dempa, Japan).

2.2 Microstructural characterization

X-ray diffraction (XRD) spectroscopy was used to analyze both the cBN precursor and sintered BN ceramics using an X-ray diffractometer (Smartlab Rigaku, Japan) equipped with Cu Kα radiation (λ = 0.154 nm), which was operated at 40 kV and 40 mA. Scans were conducted over a scanning range of 10°–100° with a step size of 0.02° and at a scan rate of 10°·min^{-1}. Raman spectra were recorded on a DXR Raman spectrometer (Thermo Fisher, USA) with a 532 nm laser. The elemental composition of the precursor and samples was analyzed by X-ray photoelectron spectroscopy (XPS) using an ESCALAB QXi spectrometer (USA) with Al Kα radiation. Energy-dispersive X-ray spectroscopy (EDS) analysis of cBN was performed using an XFlash Detector 6|60 (Bruker, Germany), integrated into a Regulus-8100 microscope (Hitachi, Japan).

Structural anisotropy is typically assessed by the IOP value, a widely recognized metric for quantifying the degree of preferred grain orientation. The IOP value was calculated from XRD peak intensities according to Eq. (1) [18,19]:

$$\mathrm{IOP}=\begin{cases}\dfrac{(I_{100}/I_{002})_{\mathrm{TS}}}{(I'_{100}/I'_{002})_{\mathrm{SS}}}, (I_{100}/I_{002})_{\mathrm{TS}} > (I'_{100}/I'_{001})_{\mathrm{SS}}\\ -\dfrac{(I'_{100}/I'_{002})_{\mathrm{SS}}}{(I_{100}/I_{002})_{\mathrm{TS}}}, (I_{100}/I_{002})_{\mathrm{TS}} < (I'_{100}/I'_{000})_{\mathrm{SS}}\end{cases} \quad (1)$$

where I_{hkl} and I'_{hkl} represent the intensities of (*hkl*) diffraction peaks for the top surface (TS) and side surface (SS), respectively. For hBN ceramics, IOP > 1 and IOP < −1 indicate that the grains exhibit preferential orientation, with the *c*-axis aligned either perpendicular or parallel to the direction of applied pressure, respectively. An IOP absolute value near 1 suggests a lack of preferred orientation, indicating a structurally isotropic ceramic.

Field-emission scanning electron microscopy (FESEM) was performed using a Regulus-8100 microscope (Hitachi, Japan) to characterize the morphology of cBN nanoparticles as well as the polished and fractured surfaces of the BN ceramics.

More detailed microstructure characterization was performed via a transmission electron microscope (TEM; Grand ARM200, JEOL) operated at an accelerating voltage of 200 kV and a scanning transmission electron microscope (STEM; ARM300, JEOL) operated at an accelerating voltage of 300 kV. For TEM sample preparation, cBN nanopowder was dispersed in anhydrous ethanol via ultrasonic treatment, drop-cast onto a carbon-coated copper grid, and subsequently dried before TEM observation. Additionally, thin foils were extracted from the as-sintered bulk samples using a focused ion beam (FIB; Helios 5 CX Dual Beam, Thermo Fisher) for TEM analysis. These foils were further thinned to less than 100 nm and polished by Ar-ion milling (NanoMill; Model 1040, Fischione) to remove surface damage.

Nitrogen adsorption/desorption isotherms were measured at −196 °C using a three-station fully automated surface area analyzer (Quantachrome Autosorb IQ3, USA). Prior to the measurements, samples were degassed under high vacuum at 300 °C for 8 h.

2.3 Density measurement

The densities of the samples were determined employing both gravimetric analysis and Archimedes' method. In the gravimetric analysis, the sample was processed into a cylinder (diameter of 3.0±0.05 mm, height of 4.5±0.05 mm). The volume (V) of the sample was obtained according to the cylinder volume equation, and the mass (m) was measured using a high-precision microbalance (MS105DU, Mettler-Toledo, Switzerland). The sample density was then calculated as $\rho = m/V$. For Archimedes' principle-based measurements, the sample density (ρ) was calculated based on the equation $\rho = [m_1/(m_1 - m_2)]\rho_l$, where m_1 is the mass of the dried sample in air; m_2 is the mass of the sample suspended in deionized water after absorbing water; ρ_l is the density of the impregnation medium (deionized water). Each sample underwent triplicate measurements with the arithmetic mean adopted as the final density value. In addition, the relative densities of all sintered samples were calculated based on the theoretical density of hBN (2.27 g·cm^{-3}).

2.4 Mechanical properties

Compressive and flexural strengths were measured at room temperature using a mechanical property testing system (MTII/Fullman SEMtester 2000, USA). Uniaxial compression tests were performed according to the Standards GB/T 8489-2006, where cylindrical samples with diameters of 3 mm and heights of 4.5 mm were prepared through precision machining and polishing. Tests were conducted at a constant strain rate of 1×10^{-4} s^{-1}. Three-point bending tests were conducted following the Standards GB/T 6569-2006 to evaluate the flexural strength. Rectangular samples with dimensions of 1 mm × 1.5 mm × 10 mm were used, supported on a span of 7 mm. A crosshead speed of 0.01 mm·min^{-1} was applied to ensure a quasi-static loading condition. Nanoindentation hardness was obtained using an NHT3 instrument (Anton Paar, Austria) equipped with a Berkovich diamond tip. Load–displacement curves, obtained under a load of 100 mN and loading, dwelling, and unloading durations of 15, 10, and 10 s, respectively, were analyzed via the Oliver–Pharr model [20] with an assumed Poisson's ratio of 0.2.

2.5 Thermal properties

Thermal conductivity (k) was calculated using the equation $k = \alpha\rho c_p$, where α is the thermal diffusivity measured by a light flash apparatus (LFA 467 MicroFlash, NETZSCH, Germany), ρ is the sample density, and c_p is the specific heat capacity determined by a differential scanning calorimeter (DSC 2500, TA Instruments, USA). To measure the thermal conductivity perpendicular to the pressing direction, the pellets were first cut into bars, rotated 90° to orient the sectional face upward, and then reassembled into a new pellet to ensure proper alignment for testing [21]. Thermal stability and oxidation resistance were assessed via both differential scanning calorimetry (DSC) and thermogravimetric analysis (TGA) by a synchronous thermal analyzer (STA 449F5, NETZSCH, Germany) over a temperature range of 200–1400 °C in air and 200–1200 °C in an argon atmosphere. The heating rate was 10 °C·min^{-1}.

3 Results and discussion

3.1 Phase transformation and microstructural evolution from cBN to hBN

The microstructure of the pretreated cBN precursor powder was characterized (Fig. 1 and Fig. S3 in the ESM). XRD analysis (Fig. 1(a)) revealed characteristic diffraction peaks of the zinc blende structure. The (111) peak was symmetrical and sharp, indicating high crystallinity of the raw cBN material. No peaks corresponding to B_2O_3 or other impurities were detected. XPS results (Figs. 1(b) and 1(c)) confirmed sp^3 hybridized B and N atoms, with B 1s and N 1s binding energies at 191.2 and 398.7 eV, respectively [22]. The absence of a B–O peak at 192.9 eV [22] indicated negligible B_2O_3 content. EDS mapping (Fig. S3(a) in the ESM) showed a homogeneous distribution of B and N with an atomic ratio of ~1 : 1 (B : N = 48.6 : 51.4). Nanoparticles tended to aggregate due to their high surface energy (Fig. S3(b) in the ESM). Individual cBN particles exhibited an island-like morphology with sharp edges and an average diameter of ~50 nm (Figs. S3(c) and S3(d) in the ESM). The selected area electron diffraction (SAED) pattern exhibited three diffraction rings corresponding to the (111), (200), and (311) planes, consistent with the XRD results (Fig. S3(d) in the ESM). The high-resolution TEM (HRTEM) image (Fig. S3(e) in the ESM) distinctly presented lattice fringes with an interlayer spacing of 0.209 nm, which aligned with the (111) plane of cBN.

Under ambient conditions, cBN is thermodynamically stable, but it transforms into hBN at elevated temperatures. To systematically investigate the phase transformation, samples sintered at 1500–1800 °C were characterized by XRD, XPS, Raman, FESEM, and HRTEM, as illustrated in Fig. 1. With increased sintering temperature, the cBN peaks weakened and disappeared, while hBN peaks emerged, indicating a phase transformation from cBN to hBN (Fig. 1(a)). At 1500 °C, cBN peaks remained prominent, and a peak near 26° corresponding to the hBN (002) plane indicated the onset of the phase transition. For nanosized cBN, the onset transformation temperature is 60–160 °C lower than that of micron-sized or bulk cBN [23]. The surface atomic composition and chemical states of the 1500BN sample were analyzed by XPS (Figs. 1(b) and 1(c)). A π-plasmon

peak was observed at ~9 eV above the B–N peak [24], confirming the presence of sp^2 bonding, which is characteristic of hBN. This finding is consistent with the XRD results. At 1600 °C, the diffraction peaks of cBN exhibited a marked weakening. Simultaneously, the (002) peak of hBN intensified, and peaks at approximately 41.6°, 43.9°, 55.2°, and 75.9° emerged, corresponding to the (100), (101), (004), and (110) planes of hBN, respectively. However, the XRD pattern of 1600BN deviated from that of typical hBN, showing expanded interlayer spacing and broader (100) and (101) peaks. These features are characteristic of tBN, where layers have random rotational and translational disorder around the *c*-axis (Fig. S1(c) in the ESM). This disorder results in an interplanar spacing of the (002) plane between 0.350 and 0.380 nm [25], while that of hBN is 0.333 nm. HRTEM analysis (Fig. 1(e)) confirmed the coexistence of cBN and tBN phases, showing distinct regions for each. At 1800 °C, the (002) peak became narrower, and the absence of cBN diffraction peaks confirmed the complete transformation to well-defined hBN. Notably, the synthesized samples, based on HRTEM images, showed no evidence of onion-like BN, in contrast to previous studies [17].

The Raman spectra of the samples further confirmed the phase transformations (Fig. 1(d)). The raw cBN showed two peaks at approximately 1043 and 1268 cm^{-1}, corresponding to the transverse optical (TO) and longitudinal optical (LO) vibration modes, respectively. Both modes are associated with the zinc blende structure of cBN. A key indicator of the phase transformation was the emergence of a peak near 1365 cm^{-1}, assigned to the in-plane B–N stretching mode (inset of Fig. 1(d)) [26]. At 1600 °C, the E_{2g} peak broadened and red-shifted, attributed to variations in domain size or structural disorder in tBN [27]. In addition, the intensity of the E_{2g} peak increased with increasing temperature, indicating an improved crystallinity of hBN.

The phase transformation from cBN to hBN was accompanied by notable morphology changes. In contrast to the sharp edges of the original cBN nanoparticles, the grains in 1600BN exhibited smoother surfaces and more diffuse boundaries (Fig. 1(f)). At this stage, hBN began to grow on the surfaces of cBN particles, but the typical flaky morphology of hBN was not fully developed [23]. In the fractured surface of 1800BN (Fig. 1(g)), the grains displayed well-defined flaky features with a lateral size of approximately 450 nm. The optical photographs in the insets of Figs. 1(f) and 1(g) show the color evolution of the samples: The intermediate phase (1600BN) was gray, in contrast to the uniformly white appearance of the fully transformed 1800BN. These observations indicated that the transformation of cBN into hBN was initiated at 1500 °C, progressed rapidly above 1600 °C, and was fully completed at 1800 °C.

3.2 Structural isotropy and sinterability

Building on the phase transformation of cBN to hBN, a series of BN ceramics was synthesized at temperatures from 1800 to 2200 °C. As shown in Fig. 2(a), the (002) diffraction peak of hBN shifted to higher angles with increasing temperature, accompanied by increased intensity and a decreased full width at half maximum (FWHM). These changes indicate improved crystallinity and grain growth. This trend is further supported by Raman spectra (Fig. 2(c)), which show that the E_{2g} peak intensity increased and its FWHM decreased. FESEM images of fracture surfaces directly revealed that the in-plane lateral size of flake-like hBN particles increased with temperature (Fig. S4 in the ESM and Fig. 2(d)), in agreement with the XRD results.

The density of the sintered bulks was lower than the theoretical

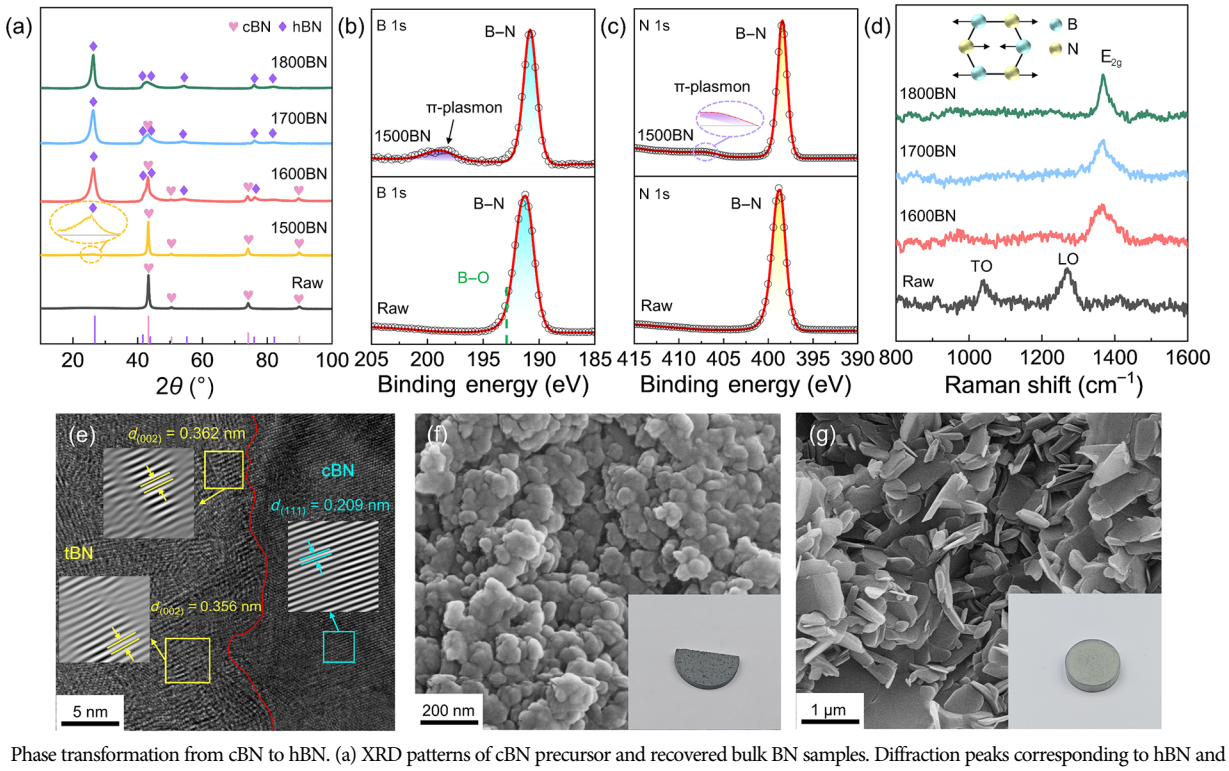

Fig. 1 Phase transformation from cBN to hBN. (a) XRD patterns of cBN precursor and recovered bulk BN samples. Diffraction peaks corresponding to hBN and cBN were indexed according to standard PDF cards of No. 34-0421 and No. 35-1365, respectively. (b, c) XPS spectra of cBN precursor and 1500BN in the B 1s and N 1s, respectively. (d) Raman spectra of cBN precursor and recovered bulk BN samples. Inset illustrates atomic vibration corresponding to E_{2g} peak. (e) HRTEM image of 1600BN. Insets show inverse fast Fourier transform (IFFT) patterns from selected boxed areas. (f, g) FESEM images of fractured surfaces of 1600BN and 1800BN, respectively. Insets show photographs of bulk BN samples with diameters of 15 mm.

density of hBN, with a relative density ranging from 67% to 82%, and increased with temperature (Fig. 2(e)). The densities of 1800BN and 1900BN were 1.53–1.57 g·cm^{-3}, which are comparable to those of hBN ceramics fabricated by pressureless sintering without aids [28–30]. In contrast, 2000BN, 2100BN, and 2200BN reached higher densities of 1.84–1.87 g·cm^{-3}, approximately 80% of the theoretical density of hBN. This abrupt rise in density between 1900BN and 2000BN suggested improved densification and sintering efficiency. Within this temperature range, the rapid diffusion of B and N atoms facilitated grain coalescence and pore elimination, as evidenced by the sharp increase in hBN particle size (from 0.63 to 5.67 μm, Fig. 2(d)) and the reduction in porosity. Nitrogen adsorption/desorption isotherms measured at −196 °C (Fig. S4(f) in the ESM) revealed characteristic type IV isotherms with H3 hysteresis loops for both the 1800BN and 2000BN samples, consistent with the presence of slit-like pores formed by the stacking of plate-like particles [31]. Notably, the hysteresis loops exhibited a progressive weakening with sintering temperature, suggesting a suppression of mesoporous structures. The pore size distribution analysis (inset of Fig. S4(f) in the ESM) further demonstrated a significant decrease in mesopore volumes in 2000BN, which correlates well with the observed increase in material density.

The unique bonding in hBN with strong in-plane covalent bonds and weak interlayer van der Waals interactions governs its sintering behavior and results in pronounced anisotropy in the resulting ceramics. This anisotropy is manifested in the differences in structure and properties between directions perpendicular and parallel to the applied sintering pressure. Figures 2(a) and 2(b) show the XRD patterns of the samples in the TS and SS, respectively. In both surfaces, a similar set of diffraction peaks corresponding to the hexagonal phase was observed. For all sintering temperatures, the calculated absolute value of IOP remained close to 1 (Fig. 2(f)), indicating randomly oriented grains and isotropic BN ceramics. Since hBN grains grow faster along the BN layer than along the interlayer direction [32], increasing the sintering temperature led to grain coarsening and a decrease in the I_{100}/I_{002} ratio in both directions. Simultaneously, the "rotation effect" under pressure became more pronounced in larger grains, orienting the *c*-axis of some grains parallel to the pressure direction and resulting in a shift of the IOP from positive to negative values [33]. Isotropic hBN ceramics were also obtained by hot-pressing cBN under conditions similar to the SPS process (sample HP-1900). To identify the critical role of the cBN precursor in achieving structural isotropy, a control sample (hBN-2200) was prepared by SPS using hBN powder as the raw material. The XRD pattern of hBN-2200 from the two surfaces exhibited significant differences (Fig. S5 in the ESM), and the calculated IOP value of 65.88 confirms a strong preferred orientation.

The SEM images directly show the grain orientation distribution. FESEM images of the polished TS and SS (Fig. S6 in the ESM) show that the BN grains have similar layered characteristics in both directions, with no preferred orientation or

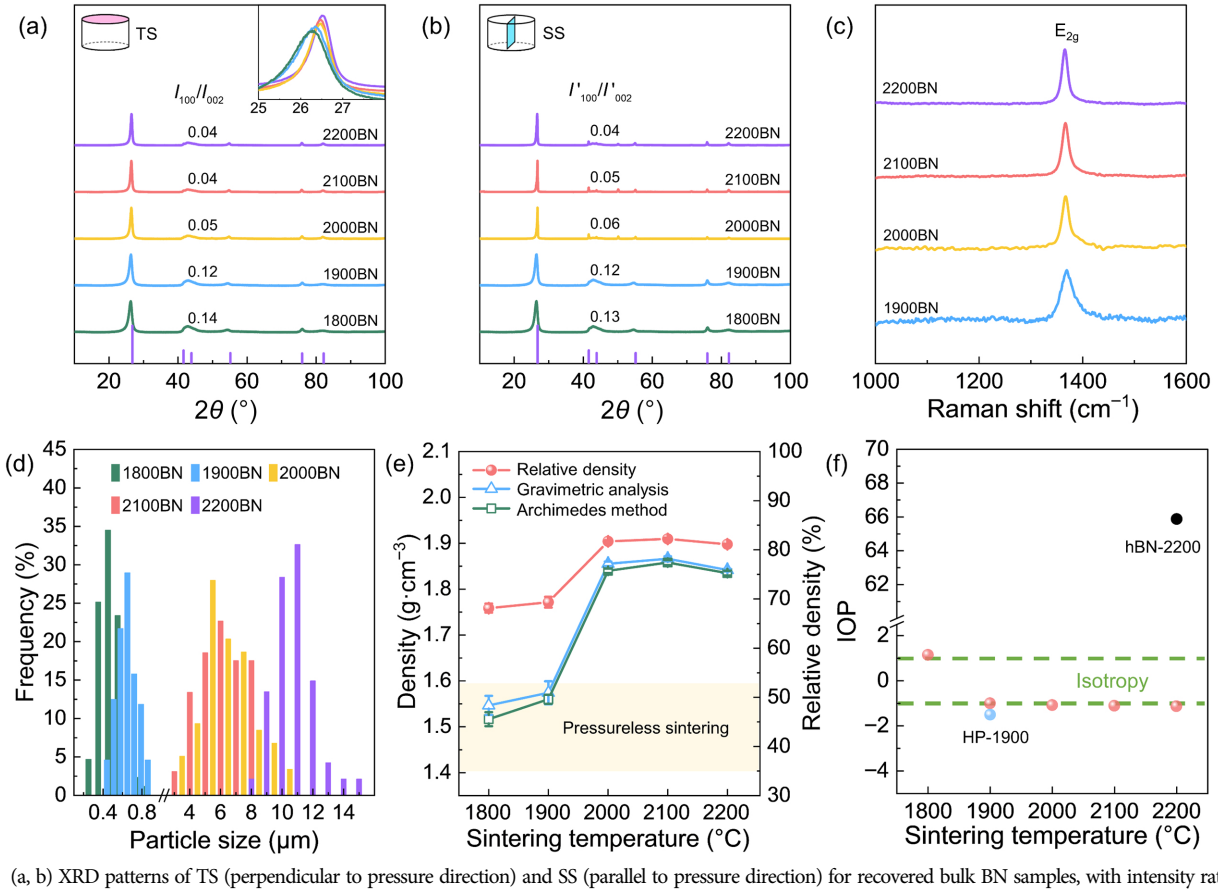

Fig. 2 (a, b) XRD patterns of TS (perpendicular to pressure direction) and SS (parallel to pressure direction) for recovered bulk BN samples, with intensity ratios of I_{100}/I_{002} and I'_{100}/I'_{002} annotated. Purple vertical lines correspond to standard PDF card (No. 34-0421) of hBN. Inset provides a magnified view of (002) diffraction peak. (c) Raman spectra of recovered bulk BN samples. (d) In-plane lateral size distribution of hBN sheets in recovered bulk BN samples, determined through statistical analysis of more than 200 particles per sample based on corresponding FESEM images. Average particle sizes for 1800BN, 1900BN, 2000BN, 2100BN, and 2200BN are 0.45, 0.63, 5.67, 6.25, and 10.28 μm, respectively. (e) Densities and relative densities of sintered ceramics at different sintering temperatures. Yellow shaded area represents density of hBN ceramics fabricated by pressureless sintering without aids. (f) IOP values of bulk BN samples.

清華大学出版社 Tsinghua University Press | SciOpen

directional dependence, further confirming the isotropic nature of the material.

3.3 Formation mechanism of isotropic microstructure

The isotropic structure of sintered BN ceramics originates from the microstructural evolution of the cBN precursor during sintering. Based on HRTEM analysis of samples sintered at various temperatures, we propose a formation mechanism for the isotropic hBN bulk, as illustrated in Fig. 3. Unlike flaky hBN powder, the cBN precursor does not exhibit preferential orientation during pre-pressing due to its grain morphology. In the initial stage of the phase transformation (~1500 °C), sp^3 bonds at the surface defects of cBN break and convert into sp^2 bonds, accompanied by atomic rearrangement that generates randomly oriented tBN, which serves as the building blocks for hBN formation. At this stage, the cBN and tBN phases coexist with a semi-coherent interface (Figs. 4(a)–4(d)), and free (111) planes with dangling bonds are observed at the edges of the cBN crystal. Notably, the cBN-to-tBN transformation occurs simultaneously across multiple areas around the cBN surface (Fig. 4(d)). The tBN phase exhibited expanded and distorted interlayer spacing, with the (002) plane spacing ranging from 0.350 to 0.352 nm. The (111) planes of cBN are aligned parallel to the (002) basal planes of sp^2-bonded tBN, with three cBN (111) planes corresponding to two tBN layers, a phenomenon also observed in the transformation between diamond and graphite [34]. This ratio closely matched the spacing ratio of cBN (0.209 nm) to hBN (0.333 nm). The formed tBN fragments encapsulated the remaining cBN core, while the stress generated by volume expansion during transformation drove the interface inward, thereby promoting further conversion.

When the temperature reaches 1800 °C, tBN fragments bond at their edges, forming large and randomly oriented hBN sheets. These sheets interlock and accumulate, forming a card-house-like structure (Fig. 4(e)) that reduces the orientation. During hBN growth, residual tBN domains attached to the surface undergo structural fluctuations [32]. As shown in Fig. 4(f), tBN fragments at the edges of hBN gradually became ordered, promoting the growth of hBN and ultimately driving the complete transformation of tBN into hBN. The newly formed hBN grains with a relatively large interlayer spacing of ~0.340 nm exhibit numerous wrinkles and dislocations due to the multi-area co-growth [32] and transformation of three cBN planes into two tBN sheets (Fig. 4(g)) [35].

Above 2000 °C, hBN grains grow rapidly, and the card-house-like structure becomes less pronounced (Fig. 4(h)). TEM observations further reveal that randomly oriented hBN sheets collide with each other during growth, leading to lattice bending and delamination (Figs. 4(i) and 4(j)). The resulting hBN grains exhibit improved crystallinity, with an interlayer spacing reduced to 0.333 nm. Some tBN remains embedded within the gaps between layers (Fig. 4(i)), acting as pinning points that hinder grain boundary migration. This pinning mechanism effectively suppressed the development of the preferred orientation in the hBN sheets [36]. Recent studies have demonstrated that larger hBN grains are more easily deflected than smaller ones under applied pressure [33]. However, hBN grains produced via cBN phase transformation are relatively small, making them less susceptible to rotation-induced effects and further lowering the degree of orientation.

3.4 Thermal conductivity

The development of vertically integrated electronic devices requires efficient three-dimensional (3D) heat dissipation, making isotropic high thermal conductivity in hBN ceramics highly desirable. Nevertheless, in single-crystalline hBN, the weak van der Waals interactions between the (002) basal planes significantly hinder cross-plane heat transfer [21]. As a result, the hBN plate is regarded as a thermal conduction barrier along the pressure direction, resulting in extremely low thermal conductivity in this direction, typically below 20 $W \cdot m^{-1} \cdot K^{-1}$ [6]. Figures 5(a) and 5(b) show the thermal conductivity and thermal diffusivity of the samples, which were measured from room temperature to 300 °C in the directions perpendicular (⊥) and parallel (//) to the sintering pressure. Owing to the isotropic microstructure, the BN bulks exhibited similar thermal diffusivity and conductivity in both directions. At room temperature, the thermal conductivities parallel to the sintering pressure direction of 1800BN, 2000BN, and 2200BN are 8.73, 34.91, and 77.46 $W \cdot m^{-1} \cdot K^{-1}$, respectively. For insulating crystals, thermal diffusivity typically decreases with temperature due to enhanced Umklapp scattering and phonon–phonon interactions [37]. The thermal conductivity of 1800BN

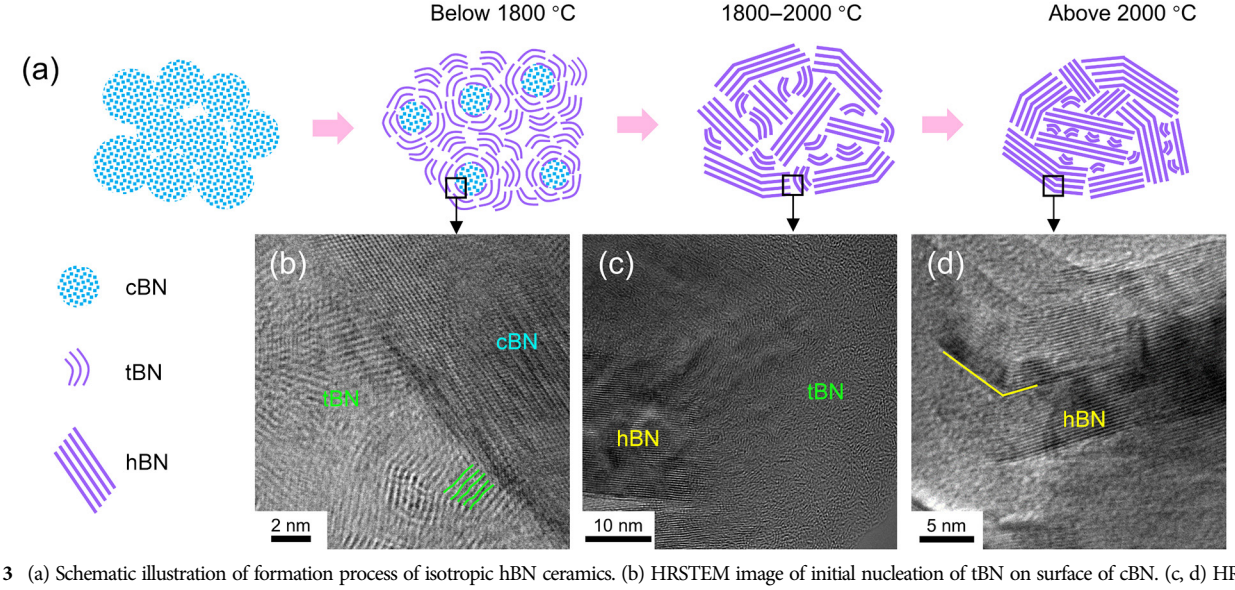

Fig. 3 (a) Schematic illustration of formation process of isotropic hBN ceramics. (b) HRSTEM image of initial nucleation of tBN on surface of cBN. (c, d) HRTEM images of residual tBN among hBN sheets and bent hBN grains.

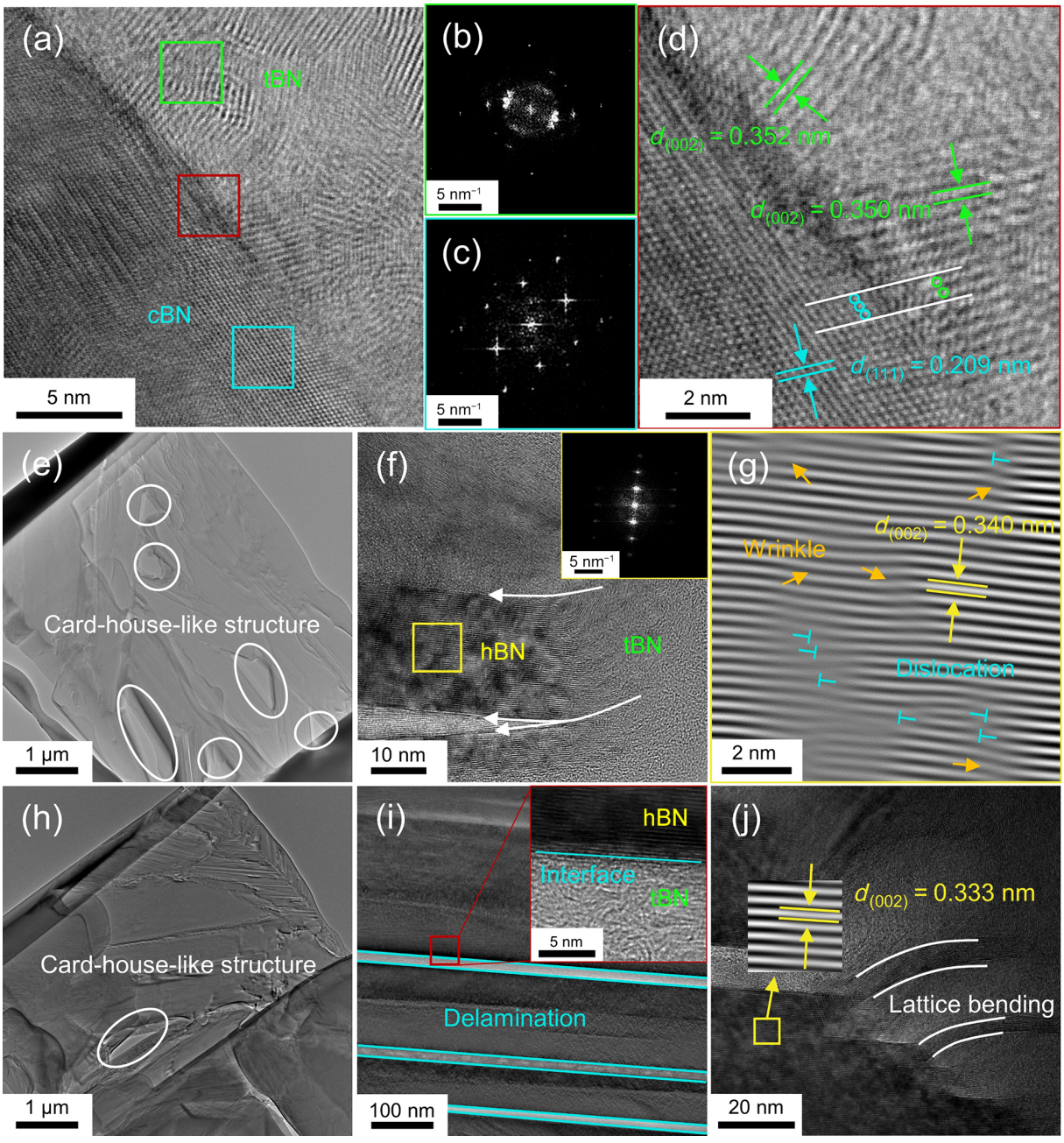

Fig. 4 (a) HRSTEM image of 1600BN, showing coexistence of cBN and tBN phases. (b, c) FFT patterns of green and blue boxed regions in (a). (d) HRSTEM image of cBN/tBN interface of red boxed region in (a). (e) TEM image of 1800BN, exhibiting card-house-like structures. (f) HRTEM of 1800BN, showing gradual crystallization of tBN into hBN. Inset shows SAED pattern of yellow boxed region. (g) IFFT image of yellow boxed region in (f), showing wrinkles (arrows) and dislocations (⊥) in newly formed hBN grain. (h) TEM image of 2200BN. (i) HRTEM image showing delamination between hBN grains. Inset shows tBN embedded between hBN layers. (j) HRTEM images showing lattice bending of hBN grains, and inset IFFT image indicating an interplanar spacing of 0.333 nm for hBN (002).

and 2000BN increases slightly with temperature, while the thermal conductivity of 2200BN exhibits a decreasing trend. This behavior results from the competing combined effects of thermal diffusivity and specific heat capacity (Fig. S7 in the ESM).

In contrast to carbon materials, where thermal conductivity is influenced by both free electrons and phonons, it is dominated by phonons in electrically insulating hBN. Therefore, any changes in its crystal structure or microstructure directly affect thermal conductivity. This is because phonon transport is governed by three kinds of scattering mechanisms, including phonon–phonon, phonon–defect, and phonon–boundary scattering [38], and the interfacial thermal resistance arising from these scattering events is the fundamental reason for the degraded thermal performance. In 1800BN, phonon–boundary scattering is the dominant mechanism due to the combined effects of the small grain size (0.45 μm) and high defect density. Additionally, the high porosity (~20%, Fig. S4(f) in the ESM) introduces numerous air/hBN interfaces, which serve as strong scattering centers owing to the significant acoustic impedance mismatch between air (thermal conductivity ~0.026 $W \cdot m^{-1} \cdot K^{-1}$) and hBN. These interfaces effectively dampen lattice vibrations and shorten the phonon mean free path, leading to a further decrease in thermal conductivity. As the sintering temperature increases, enhanced densification reduces porosity and promotes grain growth. For the 2000BN sample, the larger grain size and residual defects indicate that both phonon–boundary scattering and phonon–defect

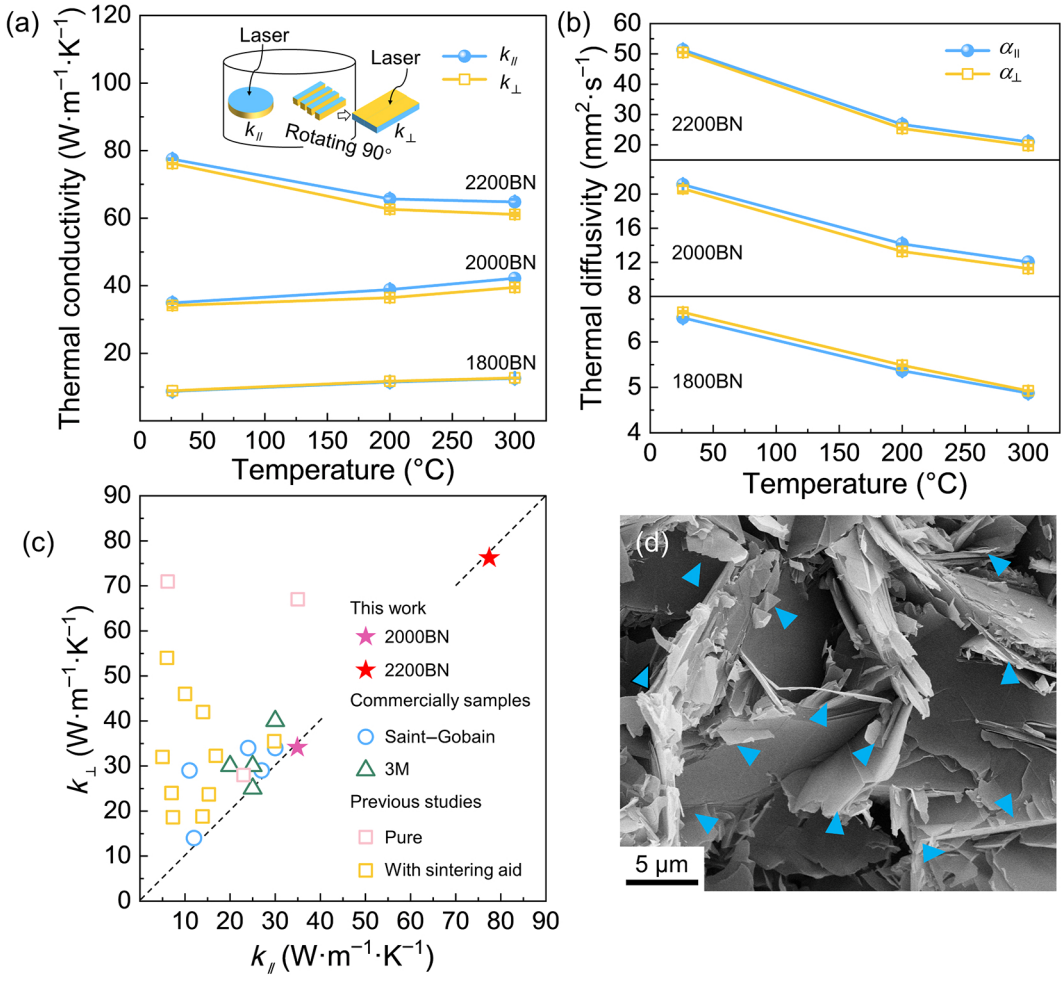

Fig. 5 Thermal properties of BN ceramics. (a, b) Thermal conductivity (k) and thermal diffusivity (α) in directions perpendicular ($\perp$) and parallel ($//$) to sintering pressure. (c) Room temperature thermal conductivity comparison of 2000BN and 2200BN with commercial BN ceramics and BN ceramics synthesized using various methods. Diagonal represents isotropic thermal conductivity. Detailed thermal conductivity data are listed in Table S1 in the ESM. (d) Fractured surface of 2200BN, showing numerous large hBN sheets (blue triangles).

scattering remain significant, but the thermal conductivity is enhanced to above 1800BN. The 2200BN sample exhibits the highest thermal conductivity, attributable to its microstructure dominated by large, well-crystallized hBN flakes (Fig. 5(d) and Fig. S8 in the ESM). This structural feature significantly reduces extrinsic scattering from pores and grain boundaries and shifts the dominant thermal-resistance mechanism to intrinsic phonon–phonon scattering. In this case, the phonon mean free path approaches the grain size, reaching its maximum extent, which accounts for the highest thermal conductivity observed in this sample.

The thermal conductivities of 2000BN and 2200BN are compared with those of commercial and literature-reported BN ceramics in Fig. 5(c) and Table S1 in the ESM. Obviously, the thermal conductivity of 2000BN and 2200BN in both directions exceeded that of the commercial BN ceramic from 3M, Saint–Gobain, and several reported hBN ceramics (Table S1 in the ESM). Notably, in the direction parallel to the sintering pressure, where conventionally sintered hBN ceramics typically exhibit lower thermal conductivity, 2200BN achieved an impressive thermal conductivity of 77.46 $W \cdot m^{-1} \cdot K^{-1}$, far surpassing that of conventional hBN ceramics.

3.5 Mechanical performance

Due to the intrinsic layered structure of single crystals, hBN ceramics often exhibit inadequate mechanical strength for structural applications when bulk materials are sintered from pure hBN powder without aids or secondary phases [39]. To evaluate the mechanical properties of isotropic hBN bulk ceramics, compressive strength and flexural strength were measured using uniaxial compression and three-point bending tests (Figs. 6(a) and 6(b)). Although higher sintering temperatures significantly enhance the thermal conductivity of hBN ceramics, their effect on mechanical strength follows a distinct trend, with 1800BN and 1900BN showing the highest strength among all samples. Additionally, 1800BN and 1900BN maintained excellent mechanical isotropy in both orthogonal directions. Specifically, 1800BN exhibited the best performance with compressive strengths of 128.88 and 129.14 MPa in the directions perpendicular and parallel to the sintering pressure, respectively, while the corresponding flexural strengths were 62.98 and 60.32 MPa, respectively. As shown in Table S2 in the ESM, 1800BN achieved superior performance to many commercial BN materials from 3M and Saint–Gobain, while its density was only 70%–80% of that of its commercial counterparts. In addition, the relationship between strength and grain size follows the Hall–Petch equation, suggesting that further reducing the grain size is expected to yield higher strength (Fig. S8 in the ESM). Nanoindentation was used to measure the hardness of synthesized bulk BN, which also showed isotropic performance in both

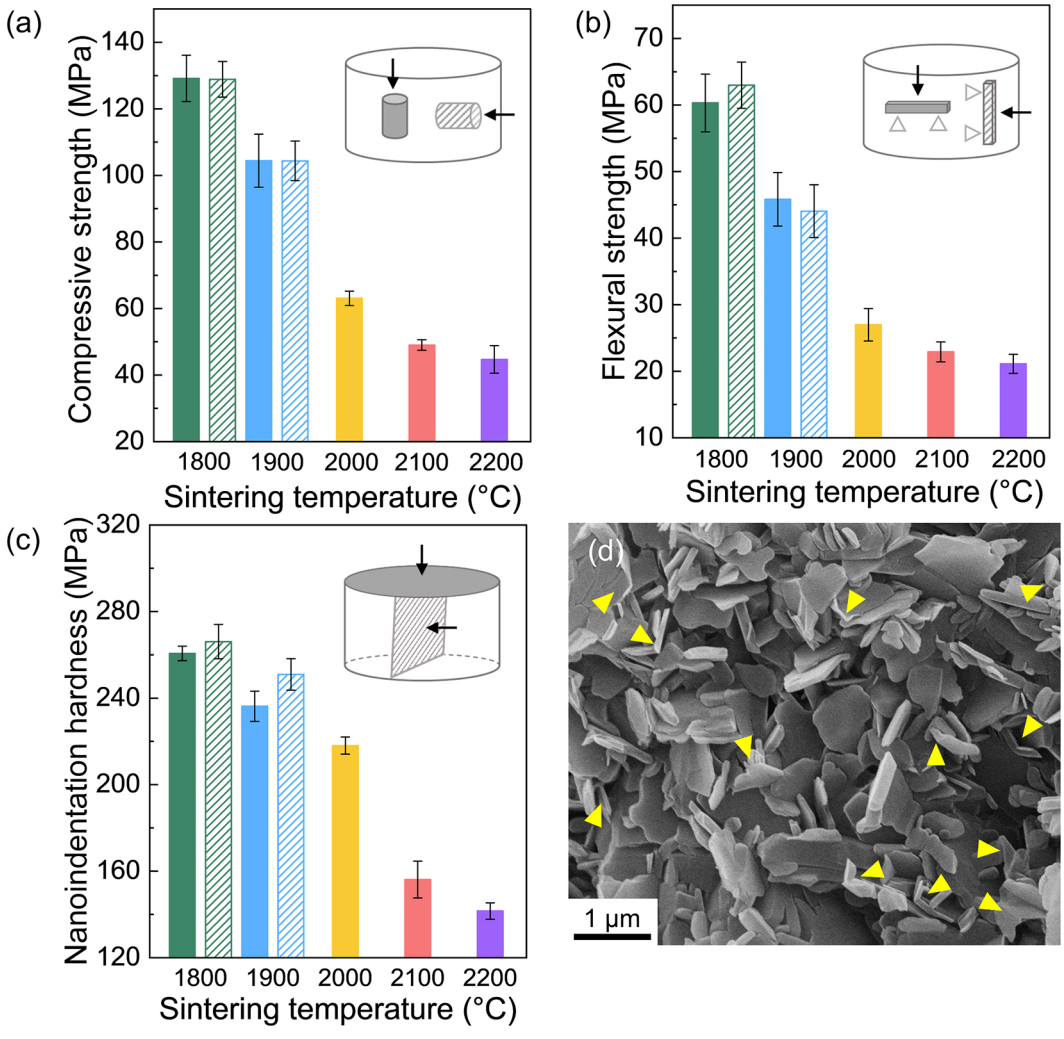

Fig. 6 Mechanical strength and hardness of BN ceramics. (a) Uniaxial compressive strength. (b) Flexural strength. (c) Nanoindentation hardness. (d) Fractured surface of 1800BN, showing bent hBN sheets (yellow triangles).

directions (Fig. 6(c)). With increasing sintering temperature, the nanoindentation hardness decreased, consistent with the trend in macroscopic mechanical strength. 1800BN exhibited the highest hardness of 273.18 MPa, which is attributed to the presence of tBN with its disordered interlayer structure. As tBN transformed into hBN at higher temperatures, the hardness of 2200BN dropped to 141.54 MPa.

To elucidate the origin of the superior mechanical performance, the fracture surfaces of the samples were examined by FESEM. As shown in Fig. S4 in the ESM, the hBN grains in the 1800BN and 1900BN samples exhibited bending deformation yet remained relatively intact (yellow triangles). These observations suggest that intergranular fracture is the predominant fracture mode for these two samples. In contrast, in the 2000BN and 2100BN samples, in addition to intact grains, a number of interlayer-dissociated grains (blue dashed circles) and fragmented flakes (blue triangles) are also discernible. This morphological feature indicates that although intergranular fracture still prevails in these two samples, a certain degree of intragranular fracture is also involved. Notably, the 2200BN sample exhibits a large quantity of BN flakes (blue triangles) derived from intragranular dissociation and fragmentation, a feature that confirms intragranular fracture as the primary fracture mode for this sample [10].

For 1800BN, the enhanced strength was attributed to the 3D interlocking network constructed by randomly oriented hBN sheets (Fig. 6(d)). Within this 3D interlocking network, the intergranular fracture mode enabled cracks to deflect repeatedly along adjacent hBN sheets with different orientations, thereby facilitating the effective dissipation and absorption of stress while suppressing interlayer sliding and dissociation within the hBN sheets [39]. At higher sintering temperatures, significant grain coarsening was observed, particularly for 2200BN (in-plane size above 10 μm), which compromised the interlocking architecture and suppressed crack deflection. These microstructural changes facilitated rapid crack propagation along the basal plane (*a*–*b* axes) through the weak interlayers of the hBN sheets. Consequently, the compressive (44.70 MPa) and flexural (21.10 MPa) strengths of 2200BN were markedly reduced.

BN is widely used as a thermally conductive and mechanically reinforcing filler in polymer composites [2,3]. However, conventional hBN fillers, typically in the form of microflakes, tend to orient during composite processing, leading to anisotropic thermal conductivity and mechanical strength [40]. This anisotropy restricts the reliability and design flexibility of components in advanced electronic and aerospace systems. Therefore, hBN derived from the transformation of cBN with an isotropic microstructure is expected to be a promising filler for achieving polymer composites with enhanced performance isotropy.

3.6 Thermal stability and antioxidant behavior

BN materials generally exhibit outstanding thermal stability and

oxidation resistance, maintaining their structural integrity up to approximately 900 °C before oxidation is initiated [41]. However, a significant challenge emerges in conventional sintering processes, where the sintering additives required to achieve higher densities frequently degrade the inherent high-temperature performance of hBN ceramics. Figures S9(a)–S9(c) present the DSC/TG curves of the 1800BN, 2000BN, and 2200BN samples heated to 1400 °C in air. The DSC curves revealed the endothermic and exothermic behavior of the material, while the TG curves demonstrated the mass variations during heating. The TG curves revealed abrupt mass gains at 991, 1063, and 1073 °C, corresponding to the formation of boron oxide [42]. Simultaneously, the DSC curves exhibited exothermic peaks at 936, 993, and 998 °C, which aligned well with the oxidation onset temperature identified by TG analysis. Compared with commercial isotropic BN ceramics (e.g., Grade HD from 3M and Grade HP from Saint–Gobain), 2200BN demonstrated an oxidation resistance temperature approximately 100 °C higher (Table S2 in the ESM). The randomly oriented hBN sheets in 2200BN effectively hindered oxygen diffusion pathways, while the larger hBN flakes reduced the density of reactive edge sites. These combined structural features synergistically enhanced the oxidation resistance. Figures S9(d)–S9(f) in the ESM display the DSC/TG curves obtained in an argon atmosphere, where no mass change was detected below 1200 °C, indicating their excellent thermal stability under inert conditions.

Given the superior mechanical and thermal properties of phase-transition-derived BN ceramics, their industrial potential was briefly assessed regarding process complexity, scalability, and raw material cost. The phase-transition route from cBN is a one-step, additive-free process that avoids sintering aids used in conventional hBN powder sintering, thus simplifying fabrication while maximally preserving the intrinsic properties of BN. Densification can be realized using standard industrial equipment, including SPS and hot-press furnaces, enabling large-scale production. Although the relatively high cost of cBN powder remains a major challenge, recent progress in hydrothermal/photochemical synthesis and recycling from waste abrasives is expected to substantially reduce production costs and improve cost-effectiveness [43–45]. Accordingly, this strategy exhibits strong prospects for industrial translation.

4 Conclusions

We have successfully synthesized isotropic hexagonal boron nitride ceramics by controlled high-temperature transformation of cBN by SPS. The thermal conversion from cBN to hBN proceeds through a tBN intermediate, leading to randomly oriented hBN sheets and a fully isotropic microstructure. The resulting ceramics exhibit isotropic mechanical and thermal properties, including a compressive strength of ~130 MPa and a thermal conductivity of ~77 $W \cdot m^{-1} \cdot K^{-1}$. The combination of high density, structural isotropy, and thermal stability demonstrates that controlling allotrope transformations offers a practical pathway to engineer BN ceramics for demanding thermal management and insulation applications. This study provides new insights into the relationship between phase transformation, microstructure, and property optimization in boron nitride ceramics and opens a promising direction for the fabrication of bulk van der Waals materials with isotropic microstructures and enhanced properties.

Acknowledgements

This work was supported by the National Natural Science Foundation of China (Nos. 52302063, 92463305, 52302048, 52202071, and 52572075), the China Postdoctoral Science Foundation (No. 2023M741879), the Beijing Natural Science Foundation (No. JR25004), the National Postdoctoral Program for Innovative Talents (No. BX20240307), the Fundamental and Interdisciplinary Disciplines Breakthrough Plan of the Ministry of Education of China (No. JYB2025XDXM403), the S&T Program of Hebei (Nos. 24461901D and 25361501D), the General programs of China Postdoctoral fund (No. 2024M762819), the Postdoctoral Fellowship Program of China Postdoctoral Science Foundation (No. GZB20240633), the Natural Science Foundation of Hebei (No. E2025203213), and the Hebei Province high-level talent funding (No. HY2025050006).

Availability of data and materials

The data that support the findings of this study are available from the corresponding author upon reasonable request.

Competing interests

The authors have no competing interests to declare that are relevant to the content of this article.

Electronic Supplementary Material

Supplementary materials are available in the online version of this article at https://doi.org/10.26599/JAC.2026.9221275.

References

[1] Yuan C, Li JH, Lindsay L, *et al.* Modulating the thermal conductivity in hexagonal boron nitride via controlled boron isotope concentration. *Commun Phys* 2019, **2**: 43.
[2] Yu G, Peng LJ, Cheng YJ. Effect of adding nano-hexagonal boron nitride–zinc oxide on the aggregated structure and properties of cross-linked polyethylene composites. *ES Mater Manuf* 2025, **30**: 1911.
[3] Wu ZJ, Wang XF, Annamareddy SHK, *et al.* Dielectric properties and thermal conductivity of polyvinylidene fluoride synergistically enhanced with silica@multi-walled carbon nanotubes and boron nitride. *ES Mater Manuf* 2023, **22**: 847.
[4] Jiang PQ, Qian X, Yang RG, *et al.* Anisotropic thermal transport in bulk hexagonal boron nitride. *Phys Rev Mater* 2018, **2**: 064005.
[5] Zhang Z, Duan XM, Qiu BF, *et al.* Preparation and anisotropic properties of textured structural ceramics: A review. *J Adv Ceram* 2019, **8**: 289–332.
[6] Zhang Z, Duan XM, Tian Z, *et al.* Texture and anisotropy of hot-pressed h-BN matrix composite ceramics with *in situ* formed YAG. *J Adv Ceram* 2022, **11**: 532–544.
[7] Duan XM, Wang MR, Jia DC, *et al.* Anisotropic mechanical properties and fracture mechanisms of textured h-BN composite ceramics. *Mat Sci Eng A—Struct* 2014, **607**: 38–43.
[8] Ni DW, Zhang GJ, Kan YM, *et al.* Textured h-BN ceramics prepared by slip casting. *J Am Ceram Soc* 2011, **94**: 1397–1404.
[9] Niu B, Cai DL, Yang ZH, *et al.* Anisotropies in structure and properties of hot-press sintered h-BN–MAS composite ceramics: Effects of raw h-BN particle size. *J Eur Ceram Soc* 2019, **39**: 539–546.
[10] Duan XM, Jia DC, Wang Z, *et al.* Influence of hot-press sintering parameters on microstructures and mechanical properties of h-BN ceramics. *J Alloy Compd* 2016, **684**: 474–480.
[11] Zhang YH, Chen JX, Zhang H, *et al.* Hexagonal boron nitride ceramic reinforced with a dispersed glass phase and microdomain-extruded glass fibers. *J Eur Ceram Soc* 2025, **45**: 117362.
[12] Toyofuku N, Yamasaki N, Kodera Y, *et al.* Turbostratic boron nitride consolidated by SPS. *J Ceram Soc Jpn* 2009, **117**: 189–193.
[13] Tian YJ, Xu B, Yu DL, *et al.* Ultrahard nanotwinned cubic boron nitride. *Nature* 2013, **493**: 385–388.
[14] Wu YJ, Zhang Y, Wang XY, *et al.* Twisted-layer boron nitride ceramic with high deformability and strength. *Nature* 2024, **626**: 779–784.

[15] Yu WJ, Lau WM, Chan SP, *et al.* *Ab initio* study of phase transformations in boron nitride. *Phys Rev B* 2003, **67**: 014108.
[16] Biswas A, Alvarez GA, Tripathi M, *et al.* Cubic and hexagonal boron nitride phases and phase boundaries. *J Mater Chem C* 2024, **12**: 3053–3062.
[17] Yang HT, Fang HL, Yu H, *et al.* Low temperature self-densification of high strength bulk hexagonal boron nitride. *Nat Commun* 2019, **10**: 854.
[18] Hubácek M, Ueki M. Effect of the orientation of boron nitride grains on the physical properties of hot-pressed ceramics. *J Am Ceram Soc* 1999, **82**: 156–160.
[19] Niu B, Cai DL, Yang ZH, *et al.* Effects of sintering temperature on the microstructure and properties of h-BN ceramics with MAS as liquid sintering aid. *Ceram Int* 2020, **46**: 1076–1082.
[20] Oliver WC, Pharr GM. An improved technique for determining hardness and elastic modulus using load and displacement sensing indentation experiments. *J Mater Res* 1992, **7**: 1564–1583.
[21] Mateti S, Yang KQ, Liu X, *et al.* Bulk hexagonal boron nitride with a quasi-isotropic thermal conductivity. *Adv Funct Mater* 2018, **28**: 1707556.
[22] Benko E, Barr TL, Hardcastle S, *et al.* XPS study of the cBN–TiC system. *Ceram Int* 2001, **27**: 637–643.
[23] Cahill JT, Du Frane WL, Sio CK, *et al.* Transformation of boron nitride from cubic to hexagonal under 1-atm helium. *Diam Relat Mater* 2020, **109**: 108078.
[24] Biswas A, Xu R, Christiansen-Salameh J, *et al.* Phase stability of hexagonal/cubic boron nitride nanocomposites. *Nano Lett* 2023, **23**: 6927–6936.
[25] Hotta M, Goto T. Densification and phase transformation of β-SiAlON–cubic boron nitride composites prepared by spark plasma sintering. *J Am Ceram Soc* 2009, **92**: 1684–1690.
[26] Geick R, Perry CH, Rupprecht G. Normal modes in hexagonal boron nitride. *Phys Rev* 1966, **146**: 543–547.
[27] Li LH, Cervenka J, Watanabe K, *et al.* Strong oxidation resistance of atomically thin boron nitride nanosheets. *ACS Nano* 2014, **8**: 1457–1462.
[28] Hagio T, Kobayashi K, Yoshida H, *et al.* Sintering of the mechanochemically activated powders of hexagonal boron nitride. *J Am Ceram Soc* 1989, **72**: 1482–1484.
[29] Hagio T, Yoshida H. Sintering and crystallization of ground hexagonal boron nitride powders. *J Mater Sci Lett* 1994, **13**: 653–655.
[30] Wang TB, Jin CC, Yang J, *et al.* Physical and mechanical properties of hexagonal boron nitride ceramic fabricated by pressureless sintering without additive. *Adv Appl Ceram* 2015, **114**: 273–276.
[31] Sing KSW. Reporting physisorption data for gas/solid systems with special reference to the determination of surface area and porosity (Recommendations 1984). *Pure Appl Chem* 1985, **57**: 603–619.
[32] Zhang Z, Duan XM, Qiu BF, *et al.* Microstructure evolution and grain growth mechanisms of h-BN ceramics during hot-pressing. *J Eur Ceram Soc* 2020, **40**: 2268–2278.
[33] Xue JX, Liu JX, Xie BH, *et al.* Pressure-induced preferential grain growth, texture development and anisotropic properties of hot pressed hexagonal boron nitride ceramics. *Scripta Mater* 2011, **65**: 966–969.
[34] Tulić S, Waitz T, Čaplovičová M, *et al.* Covalent diamond–graphite bonding: Mechanism of catalytic transformation. *ACS Nano* 2019, **13**: 4621–4630.
[35] Kuznetsov VL, Zilberberg IL, Butenko YV, *et al.* Theoretical study of the formation of closed curved graphite-like structures during annealing of diamond surface. *J Appl Phys* 1999, **86**: 863–870.
[36] Li XF, Feng YH, Liu B, *et al.* Influence of NbC particles on microstructure and mechanical properties of AlCoCrFeNi high-entropy alloy coatings prepared by laser cladding. *J Alloy Compd* 2019, **788**: 485–494.
[37] Shin S, Wang QY, Luo J, *et al.* Advanced materials for high-temperature thermal transport. *Adv Funct Mater* 2020, **30**: 1904815.
[38] Fan LW, Khodadadi JM. Thermal conductivity enhancement of phase change materials for thermal energy storage: A review. *Renew Sust Energ Rev* 2011, **15**: 24–46.
[39] Wu YJ, Zhang Y, Zhang SS, *et al.* The rise of plastic deformation in boron nitride ceramics. *Sci China Mater* 2021, **64**: 46–51.
[40] Mun HJ, Cho HB, Choa YH. High quasi-isotropic thermal conductivity of polydimethylsiloxane nanocomposites with hexagonal-boron nitride microspheres and flakes. *ACS Appl Polym Mater* 2024, **6**: 5058–5069.
[41] Haubner R, Wilhelm M, Weissenbacher R, *et al.* Boron nitrides—Properties, synthesis and applications. In: *High Performance Non-oxide Ceramics II*. Jansen M, Ed. Berlin, Heidelberg (Germany): Springer, 2002: 1–45.
[42] Jacobson N, Farmer S, Moore A, *et al.* High-temperature oxidation of boron nitride: I, monolithic boron nitride. *J Am Ceram Soc* 1999, **82**: 393–398.
[43] Yu MY, Li K, Lai ZF, *et al.* Phase-selective synthesis of cubic boron nitride in hydrothermal solutions. *J Cryst Growth* 2004, **269**: 570–574.
[44] Liu H, Jin P, Xue YM, *et al.* Photochemical synthesis of ultrafine cubic boron nitride nanoparticles under ambient conditions. *Angew Chem Int Edit* 2015, **54**: 7051–7054.
[45] Sabarinathan P, Annamalai VE. Method for recovering cubic boron nitride abrasive grains from vitrified cBN stones—A preliminary study. *Manuf Lett* 2021, **29**: 24–28.